Editors' Suggestion

Imaging the Progression of Radiolytic Damage in Molecular Crystals with Scanning Nanobeam Electron Diffraction

Ambarneil Saha,[1,*] Matthew Mecklenburg,[2] Alexander J. Pattison,[1] Aaron S. Brewster,[3] Jose A. Rodriguez,[4] and Peter Ercius[1,†]

[1]National Center for Electron Microscopy, Molecular Foundry, Lawrence Berkeley National Laboratory, Berkeley, California 94720, USA
[2]California NanoSystems Institute, University of California, Los Angeles, California 90095, USA
[3]Molecular Biophysics and Integrated Bioimaging Division, Lawrence Berkeley National Laboratory, Berkeley, California 94720, USA
[4]Department of Chemistry and Biochemistry, University of California, Los Angeles, California 90095, USA

(Received 15 July 2024; accepted 14 February 2025; published 11 April 2025)

Almost every electron microscopy experiment is fundamentally limited by radiation damage. Nevertheless, little is known about the onset and progression of radiolysis in beam-sensitive materials. Here we apply ambient-temperature scanning nanobeam electron diffraction to record simultaneous dual-space movies of organic and organometallic nanocrystals at sequential stages of beam-induced radiolytic decay. We show that the underlying mosaic of coherently diffracting domains undergoes internal rearrangement as a function of accumulating electron fluence, causing the intensities of some associated Bragg reflections to fade nonmonotonically. Furthermore, we demonstrate that repeated irradiation at a single probe position leads to the isotropic propagation of delocalized radiolytic damage well beyond the direct footprint of the incident beam. We refer to these expanding tides of amorphization as "impact craters."

DOI: 10.1103/PhysRevLett.134.146101

Introduction—Immediately as a molecular crystal is illuminated within a transmission electron microscope, it undergoes sustained bombardment with extremely harsh levels of ionizing β radiation [1]. Electrons accelerated to relativistic speeds typically deposit quantities of energy per unit mass in the range of megagrays (MGy; 10^6 J kg^{-1}) [2]. Thus, electron beam-induced radiolytic damage has long been considered the "fundamental limit" [3] constraining fields such as ultrafast electron diffraction [4], single-particle analysis [5], and 3D electron crystallography [6].

Despite its crucial impact, little is rigorously understood about the onset and progression of radiolytic damage in beam-sensitive materials, particularly in real space. If a primary inelastic collision causes electronic excitation of an atom within the specimen, many physical consequences can ensue [7]. These include inner- and valence-shell ionization, excitation and dissipation of plasmon and phonon oscillations, secondary electron emission, and homolytic scission of covalent bonds [8,9]. Arguably the most consequential downstream effect of primary excitation is the generation, diffusion, and propagation of free radicals, generally thought to occur on the picosecond timescale [8,9]. Once formed, these reactive species can diffuse throughout the specimen and spark cascades of secondary homolytic reactions. As a result, this process is often considered the predominant mechanism by which radiolytic damage destroys molecular crystals [10–12].

The typical metric used for monitoring the degradation caused by radiolysis is the disappearance of Bragg reflections in diffraction patterns [13]. Upon prolonged exposure, the intensities of Bragg spots recede into the noise floor, indicating the permanent loss of crystallinity. Several studies have analyzed the radiolytic decay of Bragg reflections in organic and biomolecular crystals [13–19]. Nevertheless, these analyses have mostly been limited to indirect observation via diffraction alone, and little is known about the physical changes within the specimen which *drive* the deterioration of Bragg spots. A *simultaneous* visualization of the effects of electron beam-induced radiolysis—in both real space and reciprocal space—remains elusive.

In this Letter, we leverage scanning nanobeam electron diffraction (NBED)—also known as 4D scanning transmission electron microscopy (4D–STEM)—to provide a dual-space perspective on this long-standing problem. 4D-STEM involves raster-scanning a focused electron probe across a user-selected region of interest in real space, partitioned into an $n \times n$ grid of scan points [20]. At each probe position in this 2D grid, an independent diffraction pattern is recorded on a backthinned CMOS-based direct electron detector operating at a frame rate of 87 kHz, corresponding to a readout speed of

*Contact author: asaha2@lbl.gov
†Contact author: percius@lbl.gov

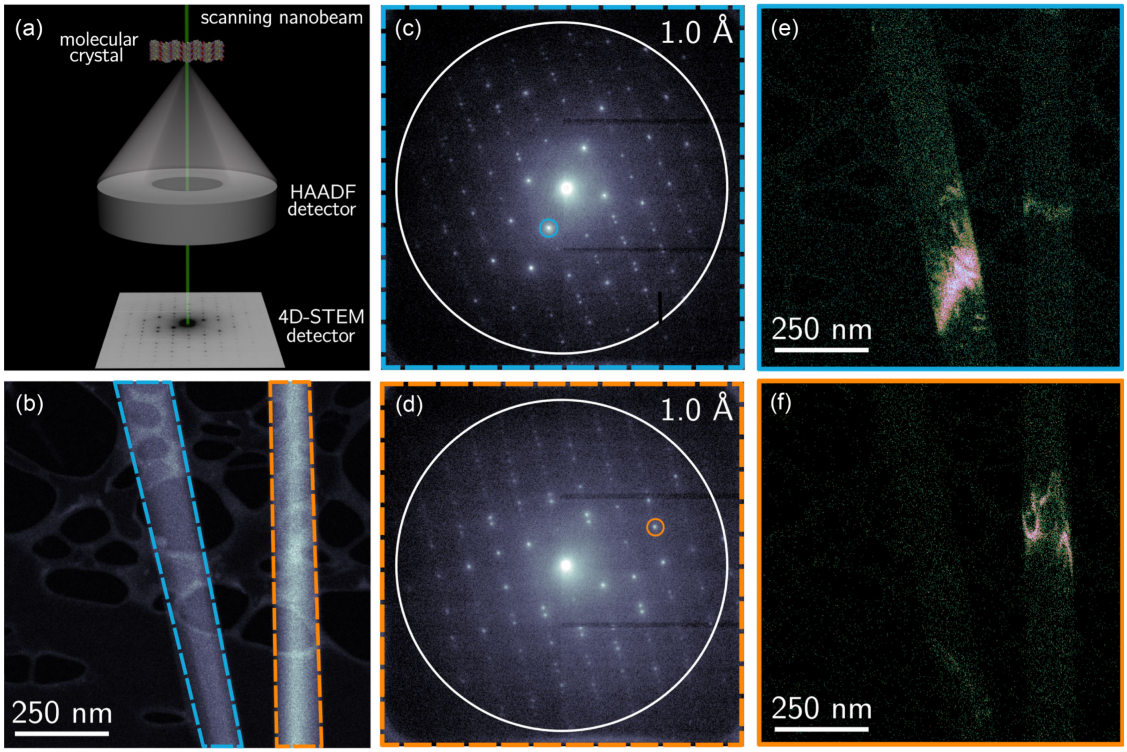

FIG. 1. Overview of scanning nanobeam electron diffraction. (a) Schematic of a 4D–STEM experiment. (b) HAADF–STEM image depicting two nanocrystals of biotin. The dashed lines superimposed on each crystal represent the boundaries of two real-space virtual apertures. (c), (d) Summed diffraction patterns exported from the regions outlined in (b) blue and orange, respectively. The blue and orange circles enclosing Bragg reflections represent reciprocal-space virtual apertures. (e), (f) Virtual dark-field images reconstructed from the Bragg reflections encircled in (c) blue and (d) orange, spatially mapping which coherently diffracting domains produced those peaks.

11 μs [21]. Simultaneously, a conventional monolithic high-angle annular dark-field (HAADF) detector is used to acquire a separate image [Fig. 1(a)]. This approach yields a four-dimensional dataset consisting of n^2 sparse diffraction patterns (indexed by reciprocal-space coordinates q_x and q_y), each linked with an associated pair of localized probe positions (x, y) in real space. By computationally summing signal from user-selected regions of a crystal [Fig. 1(b)] 4D-STEM empowers us to construct custom virtual apertures [Figs. 1(c)–1(d)] [22], functionally permitting direct visualization of exactly which coherently diffracting domains (CDDs) produced Bragg signal in reciprocal space [Figs. 1(e)–1(f)].

Furthermore, our experiments exploit recent improvements in detector sensitivity and speed [21] to add a critical fifth dimension: *time*. Rapid acquisition and live analysis of large volumes of data (e.g., up to 13200 GB) is facilitated by a unique file-transfer and data reduction pipeline involving sparsification of the raw detector frames on supercomputer nodes. This nearly lossless compression produces lightweight, MB-scale files directly viewable in our interactive graphical user interface, `DuSC_explorer` [23]. By recording a series of consecutive 4D-STEM scans on the same specimen, here we assemble dual-space movies showing that the CDDs comprising molecular crystals undergo internal rearrangement as a function of accumulating exposure to electron beam-induced radiolysis. Moreover, we demonstrate that repeated irradiation with a focused STEM probe at a single dwell point leads to the isotropic propagation of delocalized radiolytic damage—phenomena we term "impact craters."

Internal rearrangement of coherently diffracting domains—We began our studies by conducting 25 consecutive low-fluence [24] 4D-STEM experiments (0.15 e^{-}Å^{-2} scan^{-1}) at room temperature (RT) on nanocrystals of biotin (Table S1 [25]), a beam-sensitive organic molecule (Fig. S1 [25]). As long-range order in the biotin crystal was destroyed, we observed that new diffraction signal was frequently unmasked from dormant, initially Bragg-silent [33] CDDs. We found that beam-induced spatial rearrangement causes a continuously shifting array of reciprocal lattice points to intersect the surface of the Ewald sphere, leading to several distinct patterns of decay. Broadly, we classify these into two groups: monotonic and nonmonotonic decay. To identify these two groups of reflections, we generated and indexed (Fig. S2 [25]) a synthetic diffraction pattern where the intensity of each pixel represented its maximum value during the time

series [Fig. 2(a)]. We then placed virtual apertures around the centroids of 68 clearly identifiable Bragg reflections and tracked their intensities as a function of fluence [Figs. 2(b)–2(c)]. Next, we reconstructed virtual dark-field (VDF) images to visualize the corresponding real-space signal, displayed as a horizontal montage with increasing electron exposure applied from left to right [Figs. 2(d)–2(f)].

In the composite VDF images corresponding to all 68 reflections, we observed an intricate network of striated CDDs meandering across the biotin crystal, with an especially intense and long-lived swath located at the center [Fig. 2(d)]. When summing signal exclusively from the 30 reflections obeying monotonic decay, however, the central band dimmed considerably [Fig. 2(e)], unveiling a weaker group of CDDs underneath. Since reflections undergoing monotonic decay fade earlier than their nonmonotonic counterparts [Figs. 2(b)–2(c)], we reasoned that the most robust CDDs likely produce Bragg peaks inclined to experience nonmonotonic decay. As expected, the VDF images corresponding to the CDDs associated with the 38 nonmonotonically deteriorating reflections recapitulated most of the real-space signal in the central band [Fig. 2(f)]. Furthermore, a clear resolution-dependent pattern emerged: stronger, lower-resolution reflections tended to decay nonmonotonically, whereas weaker, higher-resolution reflections tended to decay monotonically [Fig. 2(a)].

After reconstructing the aggregate signal from clusters of reflections, we then moved on to case studies of individual Bragg spots. In monotonic decay, the recorded intensity for a given Bragg peak has already reached its global maximum in the first 4D-STEM scan. From this apex, it then undergoes simple, nearly linear deterioration. For instance, the twisted striation in Movie S1 [25]—corresponding to the $[\bar{2}20]$ Bragg reflection ($d = 2.36$ Å)—migrates to the right fringe of the crystal while thinning rapidly. As the intensity of this Bragg peak becomes indistinguishable from noise, its CDD fades in lockstep, indicating that reflections which undergo monotonic decay originate from CDDs which also diminish monotonically in size (Movie S1 [25]).

Conversely, in nonmonotonic decay, the global maximum of the recorded Bragg peak intensity is offset from the first scan, resulting in a delayed-onset decay pattern. These reflections represent reciprocal lattice vectors which initially do not precisely fulfill the Bragg condition. Nevertheless, their excitation error is reduced in whatever radiolysis-induced orientation the crystal has progressed to in a later scan, causing them to paradoxically appear stronger for some ephemeral period before succumbing to monotonic decay. For instance, the Friedel mate of the 2.36 Å peak considered earlier—i.e., the symmetry-equivalent reflection $[2\bar{2}0]$—follows a nonmonotonic decay pattern [Fig. 2(g)]. Although this CDD is morphologically similar to its Friedel mate, it unfurls into a more expansive striation in scans 2 and 3 relative to its shape in scan 1 (Fig. S3 [25]). Consistent with this transient boost in CDD size, reflection $[2\bar{2}0]$ also endures an extra 0.45 e^{-}Å^{-2} compared to its Friedel mate before fading (Movie S2 [25]).

Another subset of nonmonotonic decay involves Bragg spots unobservable in scan 1 which proceed to materialize midway through the dose series before deteriorating. For instance, the crescent-shaped CDD in Fig. 2(h)—corresponding to reflection $[2\bar{1}0]$—is not discernible in scan 1 and begins to form only after approximately 0.3 e^{-}Å^{-2} have been delivered (Fig. S4, Movie S3 [25]). This CDD then extends across the surface of the crystal and appears to recede into the upper-left corner as it decays. Although this 2.61 Å reflection's Friedel mate $[\bar{2}10]$ activates a similar nonmonotonic decay pattern, its lifetime is a truncated subset of its counterpart in Fig. 2(h), and its shape is not as expansive (Movie S4 [25]). This disparate behavior mirrors the asymmetry observed in the decay patterns of reflections $[2\bar{2}0]$ and $[\bar{2}20]$. At no point did an individual Bragg reflection uniformly activate the entirety of the biotin crystal, indicating clear heterogeneity [34] even at the nanoscale [35]. Although we did not physically tilt the crystal, the rotational misorientation present within the mosaic of CDDs effectively provides a pseudo-rocking curve for most Bragg reflections, mitigating the partiality of the measured intensities.

Our indexing procedure also pinpointed the presence of symmetry-forbidden Bragg reflections. For instance, [030] and $[0\bar{3}0]$ both contravene the $k \neq 2n$ extinction conditions expected in space group $P2_12_12_1$ (Fig. S2 [25]). By placing virtual apertures around these Bragg spots, we found that they both originated from closely colocalized, intense CDDs with similar band-shaped morphologies (Figs. S5–S6 [25]). Violation of systematic absences has long been recognized as evidence of multiple elastic scattering—a phenomenon previously thought to impede any prospect of accurately measuring structure-factor amplitudes due to the ensuing redistribution of diffracted intensities [6]. Nevertheless, dynamical diffraction in imperfect molecular crystals has proven far less severe than initially predicted [36]. Our 4D-STEM results suggest that certain small CDDs within otherwise highly heterogeneous molecular crystals can indeed produce detectable multiple elastic scattering, leading to the observation of symmetry-forbidden reflections. However, these effects appear limited to especially monolithic crystal subregions. When Bragg signal is blindly averaged over the many rotationally misoriented and variably ordered CDDs present in a polylithic molecular nanocrystal, dynamical character is diluted. Furthermore, as the complex internal architecture of the crystal continuously rearranges due to radiolysis, the amount of multiple elastic scattering generated by the migrating CDDs will also fluctuate, in a way that remains difficult to predict given our current level of understanding. Evidently, *en route* to total amorphization, some CDDs can reorient themselves such that their diffracting power is transiently enhanced, causing nonmonotonic

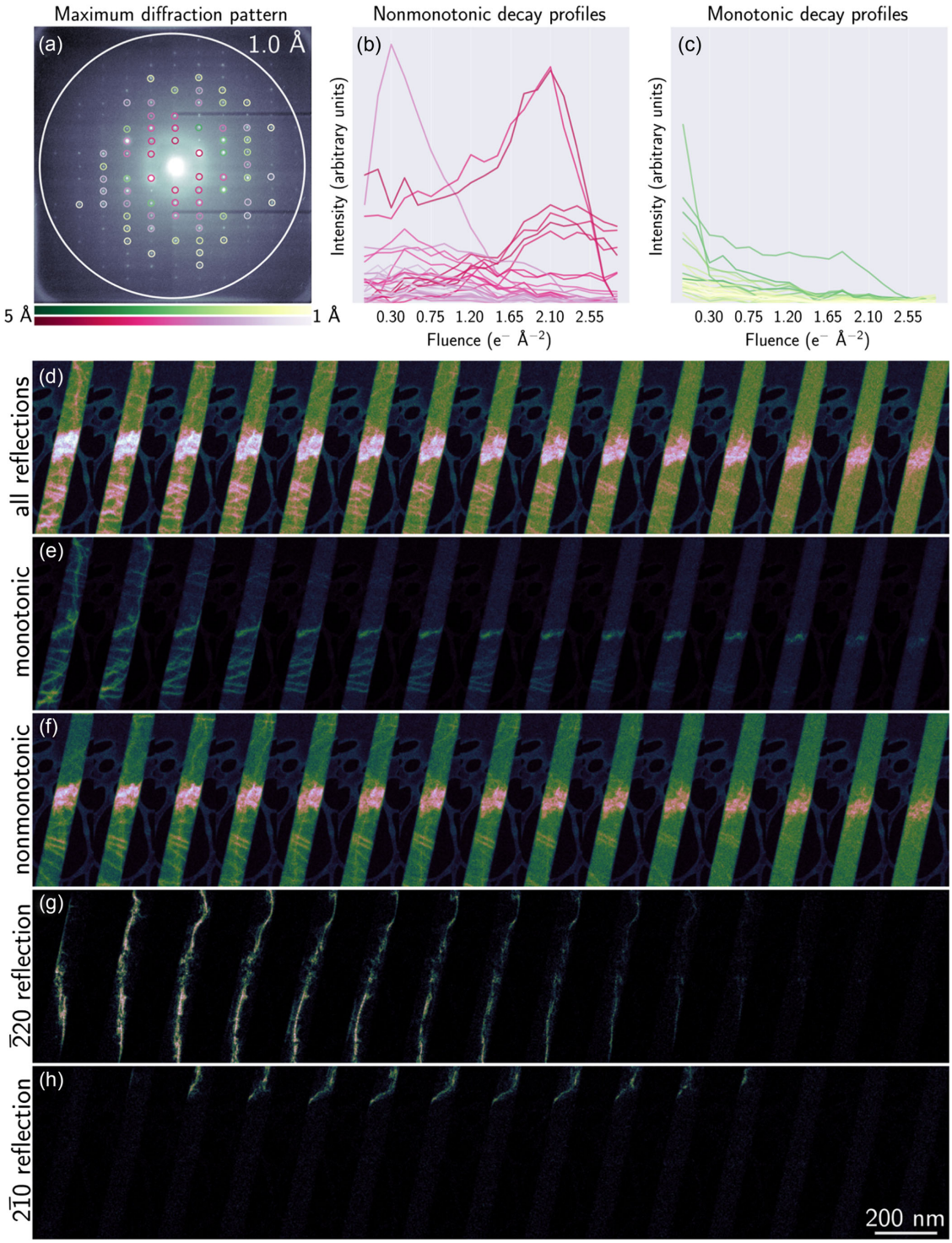

FIG. 2. Rearrangement of coherently diffracting domains in biotin. (a) Maximum diffraction pattern across all scans in the time series. (b), (c) Decay profiles of Bragg reflections undergoing (b) nonmonotonic decay and (c) monotonic decay, corresponding to the peaks encircled in (b) red and (c) green in (a). (d)–(h) Horizontal montages of VDF images reconstructed by placing reciprocal-space virtual apertures around (d) all 68 Bragg reflections identified in (a), (e) 38 Bragg reflections undergoing nonmonotonic decay, (f) 30 Bragg reflections undergoing monotonic decay, (g) a single Bragg reflection undergoing nonmonotonic decay which is present in the first scan and transiently grows stronger, and (h) a single Bragg reflection undergoing nonmonotonic decay which first becomes clearly observable in the third scan. Each VDF image represents a consecutive 4D-STEM experiment, displayed in increments of 1 (i.e., 0.15 $e^{-}\text{Å}^{-2}$ per image).

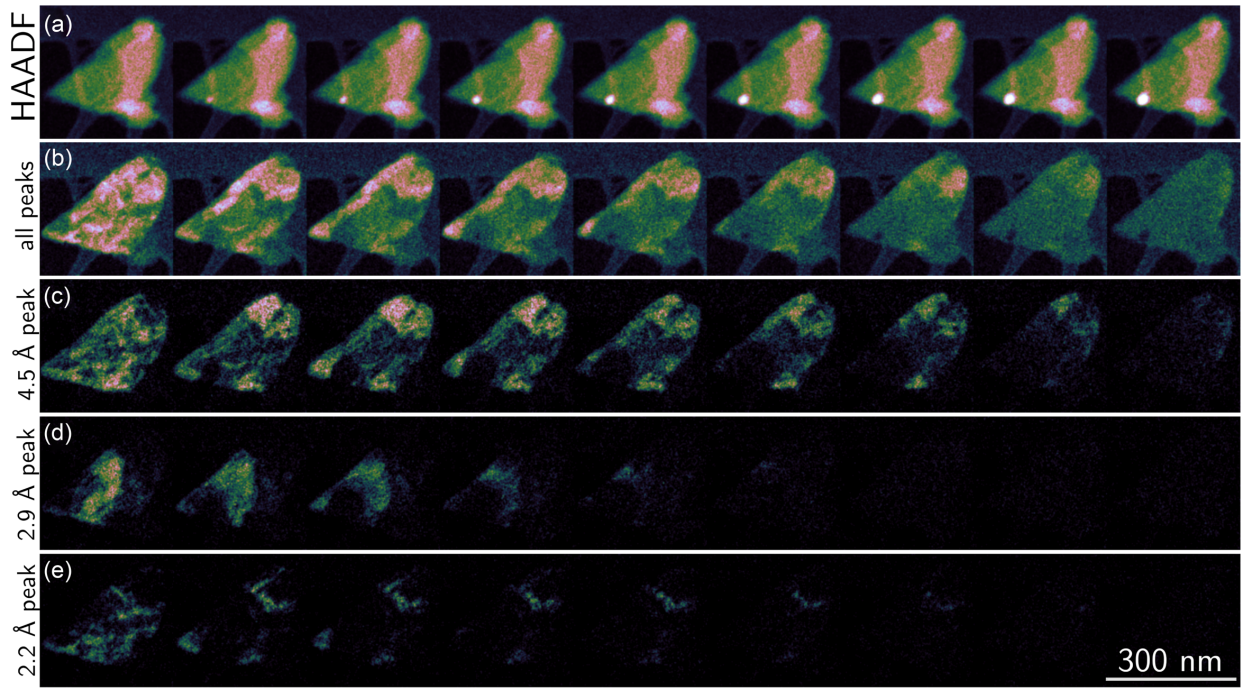

FIG. 3. Delocalized propagation of radiolytic damage in $Ni(dppf)Cl_2$. Each image represents a separate experiment, displayed in increments of 30 (i.e., 45 e^{-}Å^{-2} has been delivered between adjacent images). (a) Horizontal montage of HAADF–STEM images simultaneously acquired alongside 4D-STEM data. The steady buildup of carbon contamination is spatially colocalized with the dwell point of the probe (i.e., the epicenter of the impact crater). (b)–(e) Horizontal montages of VDF images reconstructed by placing reciprocal-space virtual apertures around (b) all clearly identifiable Bragg reflections, (c) a single 4.5 Å reflection, (d) a single 2.9 Å reflection, and (e) a single 2.2 Å reflection.

deterioration of associated Bragg spots. We emphasize that we have also recorded similar phenomena in a range of molecular crystals spanning a fairly wide gamut of chemical space, indicating that the validity of these observations extends to several other systems prone to radiolysis [37].

Delocalized propagation of damage from beam-induced impact craters—In our initial 4D-STEM scans on biotin, each probe position received an equivalent fluence, similar to the uniform illumination delivered in conventional parallel-beam TEM. We then sought to explore whether 4D-STEM could visualize the radiolytic damage caused by asymmetric delivery of incident electrons. For these experiments, we amplified the incident fluence (1.5 e^{-}Å^{-2} scan^{-1}) and switched substrates to a more beam-stable organometallic complex based on a ferrocene scaffold, $Ni(dppf)Cl_2$ (Fig. S1, Table S2 [25]). Our first experiment involved using an approximately 18 nm (full-width at half maximum) focused STEM probe to irradiate one single region of the $Ni(dppf)Cl_2$ crystal for an extra 200 ms between the acquisition of 300 consecutive 4D-STEM datasets. This created a highly localized "dead zone" in which diffraction was quickly extinguished, despite the presence of strong Bragg reflections originating from active CDDs 100 nm away from this region (Fig. S7 [25]).

Concurrently acquired HAADF–STEM images [Fig. 3(a)] showed no evidence of gross morphological changes apart from a small but steadily accumulating blot of carbon contamination at the dwell point. Intriguingly, however, the corresponding VDF images reconstructed from all Bragg peaks displayed a tide of amorphization radially propagating from this area. Our interpretation of this unexpected result is that the dead zone at the epicenter of the impact crater acts as a concentrated reservoir of reactive radiolytic fragments such as free radicals [Fig. 3(b)]. With each consecutive scan, these destructive species diffused into areas of the crystal increasingly far removed from the original source, further ablating all CDDs in their path. Each time, their advances were likely halted by molecular bulwarks such as aromatic rings, which can temporarily arrest a cascade of further radiolytic reactions via several postulated quenching pathways [38–41]. Nevertheless, since these mechanisms cannot quench propagating free radicals or secondary electrons indefinitely, each consecutive 4D-STEM scan maps the outward progression of a frontier of amorphization increasingly delocalized from the direct footprint of the incident beam.

Crucially, we then discovered that the extent of delocalization from the point of incidence also varies as a function of scattering angle. VDF images reconstructed from a series of progressively higher-resolution Bragg reflections–at 4.5 Å (Fig. 3(c), Movie S5 [25]), 2.9 Å (Fig. 3(d), Movie S6 [25]), and 2.2 Å (Fig. 3(e), Movie S7 [25]), respectively (Fig. S8 [25])—unveiled that the dimensions of the growing impact crater were larger in the latter two cases

for an identical point in the time series. CDDs producing low-resolution Bragg spots generally appear larger in size and stronger in diffracting power than their high-resolution counterparts, mostly because they correspond to a more crude level of long-range order present more uniformly throughout the crystal. Consequently, these CDDs tend to dominate the real-space signal in composite VDF images generated from all reflections. Therefore, this resolution-dependent effect is visible only when placing virtual apertures around individual peaks and is obscured when summing aggregate signal from groups of reflections.

Our physical interpretation of this phenomenon is that a small vanguard of free radicals diffuses significantly farther than the frontier delineated by the composite VDF images—on the order of tens to hundreds of nm—before being quenched. Although these species represent a minority of overall radicals produced, the smaller, weaker CDDs producing high-resolution reflections require fewer radiolytic reactions to destroy. In fact, CDDs generating high-resolution reflections frequently appear as fragmented subregions of the stronger CDDs corresponding to geometrically related low-resolution reflections, suggesting that the level of long-range order required to produce high-angle Bragg scattering is distributed much more sporadically throughout the crystal. As a result, the progress of the tide of amorphization is resolution-dependent, and the radius of the impact crater expands when reconstructing VDF images from higher-resolution Bragg reflections. Using a higher fluence, we also reproduced the delocalized propagation of amorphization in two related Pd-based organometallic complexes (Figs. S9–S10 [25]).

A counterpoint to the delocalization visualized in this Letter is provided by macromolecular x-ray crystallography. Mechanistic nuances aside, both electrons and x-rays ultimately inflict damage to molecular crystals via radiolysis [2]. Nevertheless, radiolytic damage caused by x-rays is often confined to the volume directly irradiated by the impinging quanta [42]. We attribute this discrepancy to the mismatch in size between the μm-scale FWHM of the x-ray probe and the nm-scale propagation of radiolytic damage observed in our RT scanning NBED experiments. In sum, the impact crater phenomenon is visible only when (a) the incident beam consistently delivers more ionizing radiation to one specific region of the illuminated crystal and (b) the dimensions of the probe roughly match the mean free path of whatever actively propagating reactive species is generated via radiolysis—likely dominated by free radicals at ambient temperature.

Discussion—Several analyses of electron beam-induced radiolytic damage in organic crystals have coalesced around models involving monotonic decay of Bragg peak intensities [15,19]. Nevertheless, most literature precedent exclusively monitors the fading of Bragg reflections, with no simultaneous analysis conducted in real space. Our 4D-STEM results expand this body of work by directly visualizing a crucial missing piece in this puzzle: beam-induced spatial rearrangement, driven by damaged CDDs engaging in a complex dance choreographed by radiolysis. A key consequence of this effect is that monotonic decay–the ultimate fate of every reflection—is initially coincident with an ephemeral phase where radiolytic damage reshuffles the intensities of some Bragg peaks. Subsequently, after some rotationally misoriented CDDs have been amorphized, the remainder of the crystal exhibits a more stagnant orientation, and the intensities of the associated Bragg reflections fade monotonically. We note that a judicious amount of beam-induced radiolysis could potentially anneal the initial distribution of CDDs into a more monolithic crystal, transiently producing higher-quality data [43] in the context of 3D electron crystallography (Figs. S10–S11) [25].

In 1971, Glaeser disclosed an analogous scenario involving "relative changes in diffraction intensities" upon irradiation of catalase crystals with 80 keV electrons [13]. Glaeser's hypothesis that a "significant portion of the matter within the unit cell of the structure changes to some more stable configuration" is partially consistent with our 4D-STEM data. Solely unit cell-level effects, however, cannot adequately rationalize the sudden appearance of Bragg reflections indistinguishable from background in earlier scans [Fig. 2(h)], and *ab initio* structures determined from multipass 3D ED datasets do not display drastic deviations in the root mean square deviations of atomic positions [16]. Furthermore, evidence from electron energy-loss spectroscopy (Figs. S13–S15 [25]) indicates some preservation of chemical identity even after total ablation of crystallinity [15]. Therefore, our results point more definitively to an internal reconfiguration of the CDDs themselves—i.e., at the level of crystal subregions or *ensembles* of unit cells—as the driving force behind nonmonotonic decay. Similar precedent for nonmonotonic fluctuations in Bragg peak intensities—alongside qualitatively consistent hypotheses involving real-space rearrangement—has also been found in macromolecular x-ray crystallography [44], as well as in previous SAED studies [17].

Although our setup is currently incompatible with variable-temperature experiments, future work will investigate whether CDDs which appear to deteriorate monotonically at RT may genuinely undergo some type of nonmonotonic decay at 4 or 100 K [45]. In these cases, the progression of radiolytic damage is possibly too quick to visualize at RT. Slower propagation of reactive free radicals at colder temperatures may elongate the period in which impact crater expansion and CDD rearrangement remain visible. We also anticipate our impact crater technique to provide key mechanistic insights into chemically inspired strategies to mitigate radiolytic damage, such as deuteration [46] or halogenation [47] of C–H bonds. Since these tactics seek to retard the diffusion of free radicals by increasing their mass, they could potentially cause the frontier of amorphization visualized by 4D-STEM to spread less rapidly.

Conclusion—In a landmark 1970 review, Stenn and Bahr lamented the seemingly intractable difficulties posed by radiolytic damage within the transmission electron microscope [1]. These researchers opined that "it is near impossible to follow or predict the secondary events occurring in the electron microscopic specimen because of [the] intensely complex cascading process" involved, concluding that "we shall have to be satisfied with knowing relatively little." Although the underlying phenomena remain complex, the advent of rapid [21], low-fluence 4D-STEM has enabled us to directly image the onset and progression of radiolytic damage in molecular nanocrystals, all in simultaneous dual-space detail. By unveiling the decay dynamics of CDDs associated with nonmonotonically fading Bragg reflections, these findings reshape our current understanding of radiolytic damage, paving the way for novel strategies aimed at mitigating these effects. Furthermore, our discovery of expanding impact craters at the nanoscale provides a powerful technique to visualize the delocalized spread of amorphization, building a platform for detailed mechanistic studies of radiolysis enabled by 4D-STEM.

Acknowledgments—The authors thank S. Welborn, B. Enders, C. Harris, and S. Nia for technical support, as well as R. Egerton, R. Glaeser, J. Dickerson, and E. Garman for useful discussions. Work at the Molecular Foundry was supported by the Office of Science, Office of Basic Energy Sciences, of the U.S. Department of Energy under Contract No. DE-AC02-05CH11231. This research used resources of the National Energy Research Scientific Computing Center (NERSC), a U.S. Department of Energy Office of Science user facility located at Lawrence Berkeley National Laboratory, operated under Contract No. DE-AC02-05CH11231. This work was supported by the Laboratory Directed Research and Development Program of Lawrence Berkeley National Laboratory under U.S. Department of Energy Contract No. DE-AC02-05CH11231, the BioPACIFIC Materials Innovation Platform of the National Science Foundation under Award No. DMR-1933487, and the National Science Foundation Graduate Research Fellowship (to A. S.) under Grant No. DGE-2034835. J. A. R. was supported by a Packard Fellowship, U.S. Department of Energy Grant No. DE-FC02-02ER63421, NIH-NIGMS Grant No. R35 GM128867, and the HHMI Emerging Pathogens Initiative. J. A. R. is a founder and equity stakeholder of MEDSTRUC INC.

Data availability—All 4D-STEM data are publicly accessible on Zenodo [48] and viewable using `DuSC_explorer`, our open-source python-based software.

[1] K. Stenn and G. F. Bahr, J. Ultrastruct. Res. **31**, 526 (1970).
[2] R. Henderson, Q. Rev. Biophys. **28**, 171 (1995).
[3] L. A. Baker and J. L. Rubinstein, in *Methods in Enzymology, Cryo-EM Part A Sample Preparation and Data Collection* Vol. 481, edited by G. J. Jensen (Academic Press, New York, 2010), pp. 371–388.
[4] D. Filippetto, P. Musumeci, R. K. Li, B. J. Siwick, M. R. Otto, M. Centurion, and J. P. F. Nunes, Rev. Mod. Phys. **94**, 045004 (2022).
[5] Y. Cheng, N. Grigorieff, P. A. Penczek, and T. Walz, Cell **161**, 438 (2015).
[6] A. Saha, S. S. Nia, and J. A. Rodríguez, Chem. Rev. **122**, 13883 (2022).
[7] R. F. Egerton, Micron **119**, 72 (2019).
[8] D. T. Grubb, J. Mater. Sci. **9**, 1715 (1974).
[9] D. J. Flannigan and E. J. VandenBussche, Micron **172**, 103501 (2023).
[10] Y. Talmon, in *Cryotechniques in Biological Electron Microscopy*, edited by R. A. Steinbrecht and K. Zierold (Springer, New York, 1987), pp. 64–84.
[11] J. R. Fryer, Ultramicroscopy **23**, 321 (1987).
[12] A. Meents, S. Gutmann, A. Wagner, and C. Schulze-Briese, Proc. Natl. Acad. Sci. U.S.A. **107**, 1094 (2010).
[13] R. M. Glaeser, J. Ultrastruct. Res. **36**, 466 (1971).
[14] L. Reimer and J. Spruth, Ultramicroscopy **10**, 199 (1982).
[15] P. Li and R. F. Egerton, Ultramicroscopy **101**, 161 (2004).
[16] J. Hattne, D. Shi, C. Glynn, C.-T. Zee, M. Gallagher-Jones, M. W. Martynowycz, J. A. Rodriguez, and T. Gonen, Structure **26**, 759 (2018).
[17] M. S'ari, H. Blade, R. Brydson, S. D. Cosgrove, N. Hondow, L. P. Hughes, and A. Brown, Mol. Pharm. **15**, 5114 (2018).
[18] E. J. VandenBussche and D. J. Flannigan, Nano Lett. **19**, 6687 (2019).
[19] K. Naydenova, A. Kamegawa, M. J. Peet, R. Henderson, Y. Fujiyoshi, and C. J. Russo, Ultramicroscopy **237**, 113512 (2022).
[20] K. C. Bustillo, S. E. Zeltmann, M. Chen, J. Donohue, J. Ciston, C. Ophus, and A. M. Minor, Acc. Chem. Res. **54**, 2543 (2021).
[21] P. Ercius, I. J. Johnson, P. Pelz, B. H. Savitzky, L. Hughes, H. G. Brown, S. E. Zeltmann, S.-L. Hsu, C. C. S. Pedroso, B. E. Cohen, R. Ramesh, D. Paul, J. M. Joseph, T. Stezelberger, C. Czarnik, M. Lent, E. Fong, J. Ciston, M. C. Scott, C. Ophus, A. M. Minor, and P. Denes, Microsc. Microanal. **30**, 903 (2024).
[22] C. Gammer, V. Burak Ozdol, C. H. Liebscher, and A. M. Minor, Ultramicroscopy **155**, 1 (2015).
[23] The reader is strongly encouraged to visit the relevant Zenodo repository, install `DuSC_explorer`, and interactively view our data, https://github.com/ercius/DuSC_explorer.
[24] Fluence is defined as the number of particles delivered per unit area (e^{-}Å^{-2}). This term is often conflated with dose, which is properly defined by the International System of Units as the energy absorbed per unit mass (J kg^{-1}) upon exposure to ionizing radiation.
[25] See Supplemental Material at http://link.aps.org/supplemental/10.1103/PhysRevLett.134.146101, which includes Refs. [26–32], for additional information.
[26] W. Kabsch, Acta Crystallogr. Sect. D **66**, 125 (2010).

[27] H. Fujita and Y. Kawasaki, Jpn. J. Appl. Phys. **5**, 788 (1966).
[28] P. B. Hirsch and M. J. Whelan, Phil. Trans. R. Soc. A **252**, 499 (1997).
[29] K. Diederichs and P. A. Karplus, Nat. Struct. Mol. Biol. **4**, 269 (1997).
[30] J. A. Hachtel, J. Huang, I. Popovs, S. Jansone-Popova, J. K. Keum, J. Jakowski, T. C. Lovejoy, N. Dellby, O. L. Krivanek, and J. C. Idrobo, Science **363**, 525 (2019).
[31] G. Winter, J. Beilsten-Edmands, N. Devenish, M. Gerstel, R. J. Gildea, D. McDonagh, E. Pascal, D. G. Waterman, B. H. Williams, and G. Evans, Protein Sci. **31**, 232 (2022).
[32] J. L. Dickerson, P. T. N. McCubbin, J. C. Brooks-Bartlett, and E. F. Garman, Protein Sci. **33** (2024).
[33] Our use of the term Bragg-silent means Bragg-silent with respect to a particular reflection or group of reflections; i.e., that volume of matter no longer produces the same Bragg peak(s) as it once did. Nevertheless, that particular 3D volume could still viably produce other Bragg reflections—it has not necessarily lost all long-range order altogether.
[34] T. J. Boggon, J. R. Helliwell, R. A. Judge, A. Olczak, D. P. Siddons, E. H. Snell, and V. Stojanoff, Acta Crystallogr. Sect. D **56**, 868 (2000).
[35] M. Gallagher-Jones, C. Ophus, K. C. Bustillo, D. R. Boyer, O. Panova, C. Glynn, C.-T. Zee, J. Ciston, K. C. Mancia, A. M. Minor, and J. A. Rodriguez, Commun. Biol. **2**, 1 (2019).
[36] T. Latychevskaia and J. P. Abrahams, Acta Crystallogr. Sect. B **75**, 523 (2019).
[37] A. Saha, Adventures in 3D electron crystallography, Ph.D. thesis, University of California, Los Angeles, 2023.
[38] P. Alexander and A. Charlesby, Nature (London) **173**, 578 (1954).
[39] F. G. Liming and W. Gordy, Proc. Natl. Acad. Sci. U.S.A. **60**, 794 (1968).
[40] S. D. Lin, Radiat. Res. **59**, 521 (1974).
[41] A. Howie, F. J. Rocca, and U. Valdrè, Philos. Mag. B **52**, 751 (1985).
[42] C. Schulze-Briese, A. Wagner, T. Tomizaki, and M. Oetiker, J. Synchrotron Radiat. **12**, 261 (2005).
[43] R. L. Owen, N. Paterson, D. Axford, J. Aishima, C. Schulze-Briese, J. Ren, E. E. Fry, D. I. Stuart, and G. Evans, Acta Crystallogr. Sect. D **70**, 1248 (2014).
[44] M. Warkentin, J. B. Hopkins, R. Badeau, A. M. Mulichak, L. J. Keefe, and R. E. Thorne, J. Synchrotron Radiat. **20**, 7 (2013).
[45] B. E. Bammes, J. Jakana, M. F. Schmid, and W. Chiu, J. Struct. Biol. **169**, 331 (2010).
[46] T. W. Chamberlain, J. Biskupek, S. T. Skowron, P. A. Bayliss, E. Bichoutskaia, U. Kaiser, and A. N. Khlobystov, Small **11**, 622 (2015).
[47] D. J. Smith, J. R. Fryer, and R. A. Camps, Ultramicroscopy **19**, 279 (1986).
[48] A. Saha and P. Ercius, Multiscan 4D-STEM datasets on molecular crystals: biotin and Ni(dppf)Cl_2, Zenodo (2023), 10.5281/zenodo.10387146.